Nano Research 2017, 10(9): 3113–3123
DOI 10.1007/s12274-017-1528-0
Research Article

ISSN 1998-0124
CN 11-5974/O4

Two-photon-excited near-infrared emissive carbon dots as multifunctional agents for fluorescence imaging and photothermal therapy

Minhuan Lan[1,§], Shaojing Zhao[1,§], Zhenyu Zhang[1], Li Yan[1], Liang Guo[2], Guangle Niu[2], Jinfeng Zhang[1], Junfang Zhao[2], Hongyan Zhang[2], Pengfei Wang[2,3] (✉), Guangyu Zhu[4], Chun-Sing Lee[1], and Wenjun Zhang[1] (✉)

[1] *Center of Super-Diamond and Advanced Films (COSDAF), Department of Physics and Materials Science, City University of Hong Kong, Hong Kong, China*
[2] *Key Laboratory of Photochemical Conversion and Optoelectronic Materials, Technical Institute of Physics and Chemistry, Chinese Academy of Sciences, Beijing 100190, China*
[3] *School of Future Technology, University of Chinese Academy of Sciences, Beijing 100049, China*
[4] *Department of Biology and Chemistry, City University of Hong Kong, Hong Kong, China*
[§] *Minhuan Lan and Shaojing Zhao contributed equally to this work.*

Received: 8 November 2016
Revised: 8 February 2017
Accepted: 9 February 2017

KEYWORDS

carbon dots,
phototheranostic agent,
two-photon excitation,
NIR emission,
photothermal conversion

ABSTRACT

C dots (CDs) have shown great potential in bioimaging and phototherapy. However, it is challenging to manipulate their fluorescent properties and therapeutic efficacy to satisfy the requirements for clinic applications. In this study, we prepared S, Se-codoped CDs via a hydrothermal method and demonstrated that the doping resulted in excitation wavelength-independent near-infrared (NIR) emissions of the CDs, with peaks at 731 and 820 nm. Significantly, the CDs exhibited a photothermal conversion efficiency of ~58.2%, which is the highest reported value for C nanostructures and is comparable to that of Au nanostructures. Moreover, the CDs had a large two-photon absorption cross section (~30,045 GM), which allowed NIR emissions and the photothermal conversion of the CDs through the two-photon excitation (TPE) mechanism. *In vitro* and *in vivo* tests suggested that CDs can function as new multifunctional phototheranostic agents for the TPE fluorescence imaging and photothermal therapy of cancer cells.

1 Introduction

Phototheranostics combine the diagnosis and subsequent treatment of a disease using a single-agent system. As a novel clinical solution, phototheranostics have demonstrated great potential for the early detection and rapid treatment of diseases such as cancers [1–3]. Various phototheranostic agents (PTAs) have been

---

Address correspondence to Wenjun Zhang, apwjzh@cityu.edu.hk; Pengfei Wang, wangpf@mail.ipc.ac.cn

developed in recent years, including porphyrin, phthalocyanines, and bacteriochlorin derivatives [4]. These agents rely mainly on their photoluminescence and photodynamic therapy (PDT) capabilities for phototheranostic applications [5]. Although PDT has been approved for clinical use, its efficiency is limited by factors such as the reduced partial O pressure in tumor tissues, the short lifetime, and the limited diffusion distance of reactive O species (ROS) inside the cells [6, 7]. In contrast, photothermal therapy (PTT), which employs hyperthermia generated by light-irradiated photosensitizers (PSs) to heat cancer cells, has emerged as a useful alternative for treating hypoxic tumors owing to its O-independent nature [8]. Thus far, Au nanostructures and near-infrared (NIR) organic dyes, such as indocyanine green and IR780 [9–11], have exhibited promising fluorescence-imaging and PTT performance both *in vitro* and *in vivo*. However, their biocompatibility, biodegradability, photothermal conversion efficiency, photostability, and chemical stability must be improved for their phototheranostic applications [12–14].

Recently, we demonstrated that C dots (CDs) are a unique system with both diagnostic fluorescence imaging and PDT/PTT functions [15, 16]. Compared with the aforementioned PTAs, CDs have excellent biocompatibility, broad absorption, tunable emission, and high photostability and chemical stability, making them advantageous for biomedical applications [17–20]. However, the photothermal conversion efficiency of CDs (~38.5%) is significantly lower than that of Au-based nanostructures (~60%) and must be improved to satisfy clinical requirements [21–24]. Although a high photothermal conversion efficiency of 53.2% was recently reported for oxidized N-doped CDs (supra-carbon nanodots), no fluorescence was observed from them [25]. The excitation and emission of CDs occurs mainly in the visible-light region (<700 nm), which limits their clinical applicability for the diagnosis and treatment of topical lesions. NIR emissions were observed from CDs in some studies but only in the excitation wavelength-dependent fluorescence mode; in this case, the small difference between the excitation and emission wavelengths degrades the fluorescence imaging performance [26–28].

Two-photon excitation (TPE) is a promising strategy for extending the functional window of CDs to the NIR region, and its nonlinear excitation mechanism allows a higher spatial resolution of imaging and reduces the photobleaching of CDs compared with one-photon excitation (OPE) [29]. Polyethylene glycol-passivated CDs have exhibited strong luminescence under 800-nm pulse laser excitation with a large two-photon absorption (TPA) cross section [30]. The TPE of CDs has been employed to indirectly excite organic PSs conjugated with the CDs, where the PSs were excited through Förster resonance energy transfer, and the ROS generation and PDT efficiency of the composite was dominated by the organic PS component [31, 32]. Although there have been a few reports on the ability of CDs to absorb and convert light into heat under TPE, the low photothermal conversion efficiency and visible light emission limited the *in vivo* phototheranostic performance [33]. In this study, the co-doping of CDs with S and Se yielded excitation wavelength-independent NIR emission in both the OPE and TPE modes. Significantly, the CDs exhibited excellent photostability and biostability, a large TPA cross section (~30,045 GM), and the highest photothermal conversion efficiency reported thus far for C nanostructures (~58.2%, which is comparable to that of Au nanostructures). *In vitro* and *in vivo* experiments demonstrated that the S, Se-codoped CDs can be used as multifunctional PTAs for cancer therapy through the TPE mechanism.

2 Experimental

2.1 Preparation of CDs

The CDs were prepared via the hydrothermal treatment of polythiophene (PT2) and diphenyl diselenide in an alkaline solution. The synthesis of PT2 is detailed in our previous report. In a typical procedure, for the synthesis of CDs, 10 mg of PT2 and 10 mg of diphenyl diselenide were dispersed in 15 mL of a NaOH aqueous solution (0.5 mM). The mixture was transferred into an autoclave and heated at 180 °C for 24 h. After cooling to room temperature, the CDs were collected through sequential filtration, centrifugation, and dialysis purification. They were then dispersed in water for further characterization and use.

2.2 Sample characterizations

Transmission electron microscopy (TEM) and high-resolution TEM (HRTEM) images were acquired using an electron microscope (Philips CM200). Atomic force microscopy (AFM) images were obtained using an atomic force microscope (MultiMode Nano-Scope IIIa) in the tapping mode. X-ray photoelectron spectroscopy (XPS) was performed using a surface-analysis system (VG ESCALAB 220i-XL). Fourier transform infrared spectroscopy (FT-IR) was performed using a spectrometer (IFS 66 V/S, Bruker). The zeta-potential and dynamic light scattering (DLS) spectra were recorded using a Zeta-size 3000 HS (Malvern, UK).

2.3 Optical properties measurements

The absorption spectra and OPE fluorescence spectra of the CD aqueous solution were recorded using a Shimadzu 1700 spectrophotometer and a HITACHI F-4600 spectrophotometer, respectively. TPE fluorescence spectroscopy was performed using a fiber spectrometer (USB2000 CCD, Ocean Optics). A Ti:sapphire femtosecond laser (Spitfire, Spectra-Physics, 100 fs, 80 MHz) was used as the TPE laser source. The wavelength of the output laser beam was tuned to 880 nm. The TPA cross section of the CDs in water was determined using the TPE fluorescence method. Using fluorescein in water (pH = 11) as a reference, the TPA cross section of the CDs was calculated according to the following equation

$$\sigma_{\mathrm{S}} = \frac{F_{\mathrm{S}}}{F_{\mathrm{R}}} \frac{\varphi_{\mathrm{R}}}{\varphi_{\mathrm{S}}} \frac{\eta_{\mathrm{R}}}{\eta_{\mathrm{S}}} \frac{C_{\mathrm{R}}}{C_{\mathrm{S}}} \sigma_{\mathrm{R}} \tag{1}$$

where the subscripts R and S represent the fluorescein and CDs, respectively; F is the integral area of the TPE fluorescence spectrum; φ is the OPE fluorescence quantum yield; η is the overall fluorescence collection efficiency of the experimental apparatus; and C is the concentration.

2.4 Cell apoptosis and necrosis assay

The cytotoxicity of the CDs was evaluated by analyzing the apoptosis and necrosis of HeLa cells. The cells were pre-seeded in 24-well cell culture plates and then treated with the CDs (40 μg/mL) for 4 h. After washing with a phosphate-buffered saline (PBS) solution, the cells were irradiated by a 635-nm laser for 10 min. Then, the cells were cultured for 2 h, followed by staining with Annexin V-FITC (fluorescein isothiocyanate) and PI (propidium iodide). The labeled cells were analyzed via flow cytometry using a flow cytometer (FACSCalibur).

2.5 Cell imaging

The HeLa cells were incubated with CDs (20 μg/mL) at 37 °C for 8 h. They were washed with the PBS solution three times and then visualized using a Nikon laser scanning confocal microscope (ARsiMP) under laser excitation at 488 nm (for OPE) or 880 nm (for TPE). To monitor the TPE PTT performance *in situ*, the cells cultured with and without CDs were continuously irradiated by the 880-nm laser using the laser scanning confocal microscope for 3 min.

2.6 Photothermal performance evaluation

For the assessment of the photothermal performance of the CDs, a 635-nm laser was used as the light source to irradiate aqueous solutions (1 mL) with different concentrations of CDs (0, 40, 80, and 160 ppm) in a quartz cuvette. A digital thermometer (HH12) was used to record the temperature changes of the CD solution. To evaluate the photothermal conversion efficiency, the CD dispersion (~20 ppm) was continuously illuminated by a 635-nm laser with a power of 2 W/cm^2 until a steady temperature was reached. After the irradiation was switched off, the temperature decrease was monitored to determine the rate of heat transfer from the system. The photothermal conversion efficiency, η, was calculated using the following equation

$$\eta = \frac{hS(T_{\max} - T_{\mathrm{Surr}}) - Q_{\mathrm{Dis}}}{I(1-10^{-A_{635}})} \tag{2}$$

where h is the heat-transfer coefficient, S is the surface area of the container, $T_{\max}$ is the equilibrium temperature, T_{Surr} is room temperature, Q_{Dis} is the heat dissipation due to the light absorbed by the quartz sample cell, I is the laser power, and A_{635} is the absorbance of the CD solution at 635 nm. The value of hS was derived according to the following equation

$$\tau_{\mathrm{S}} = \frac{m_{\mathrm{D}} C_{\mathrm{D}}}{hS} \tag{3}$$

Here, τ_s is the sample system time constant, and m_D and C_D are the mass (1.0 g) and heat capacity (4.2 J/g) of deionized water, respectively.

2.7 *In vivo* biocompatibility and histopathological behavior

Two groups of mice (five mice in each group) were intravenously injected with the CD aqueous solution (80 μL, 1 mg/mL) and PBS (control group), separately. After 14 d, blood samples were collected from the mice and analyzed. The major organs of the mice—including the hearts, livers, spleens, lungs, and kidneys—were harvested and washed with PBS. These organs were then stained with hematoxylin and eosin (H&E) for the detection of changes in the cellular integrity and tissue morphology.

2.8 Tumor model for IR thermal imaging and PTT

The animal experiments were performed in accordance with the guidelines for animal use and care of the Institute of Process Engineering, Chinese Academy of Sciences. The mice were inoculated subcutaneously with 4T1 cells for 7 d. When the tumors in the mice had grown to 5–10 mm in diameter, the mice were randomly allocated into treatment and control groups. The mice were intratumorally injected with 80 μL of the CD solution (1 mg/mL) or saline. After 1 h, the mice were exposed to 880-nm NIR laser (500 mW) irradiation for 10 min. During the laser treatment, full-body IR thermal images were obtained using a Fluke Ti400 IR Camera. The tumor sizes were measured every other day using a caliper, and the tumor volume was calculated using the formula $V = a \times b^2/2$, where a and b are the length and width of the tumor, respectively.

3 Results and discussion

3.1 Preparation and characterization of CDs

S, Se-codoped CDs were prepared via the hydrothermal treatment of polythiophene (PT2, whose synthesis is detailed in our previous report [34]) and diphenyl diselenide in the presence of NaOH, as shown in Scheme 1. The CDs had a mean diameter of ~20 nm, according to the TEM image and DLS analysis (Fig. 1(a) and Figs. S1(a) and S1(b) in the Electronic Supplementary Material (ESM)). The HRTEM image (inset in Fig. 1(a)) confirms the crystalline nature of the CDs, indicating an interplanar distance of 0.24 nm (corresponding to the (100) planes of graphitic C) [35]. AFM revealed that the height of the CDs was ~4 nm (Fig. 1(b)), suggesting that they had a platelet morphology.

According to the XPS survey spectrum, the CDs contained C, N, O, S, and Se with atomic ratios of 78.92% (C), 0.58% (N), 12.79% (O), 6.57% (S), and 1.13% (Se) (Fig. 1(c)). Deconvolution of the high-resolution C1s XPS spectrum (Fig. 1(d)) revealed peaks at 284.8, 285.4, 286.3, and 287.4 eV, which correspond to C–C, C–N/C–S/C–Se, C–O, and C=O bonding, respectively. The high-resolution N1s, S2p, and Se3d spectra shown in Fig. S2 in the ESM confirm the C–N, C–S, and C–Se bonding, which indicates the incorporation of S and Se atoms into the CDs. The FT-IR spectra shown in Fig. S3 of the ESM provide additional evidence of these functional groups. The zeta potential of the CD aqueous solution was determined to be +47.8 mV (Fig. S1(c) in the ESM), indicating the positive surface charging of the CDs, which was probably due to the surface ammonium termination.

3.2 Optical properties of CDs

As shown in Fig. 2(a), the ultraviolet–visible (UV–vis) absorption spectrum of the CDs in the aqueous solution reveals that the CDs had broad absorption from 350 to 750 nm with a maximum at ~526 nm. The CDs exhibited two emission peaks at ~731 and 820 nm

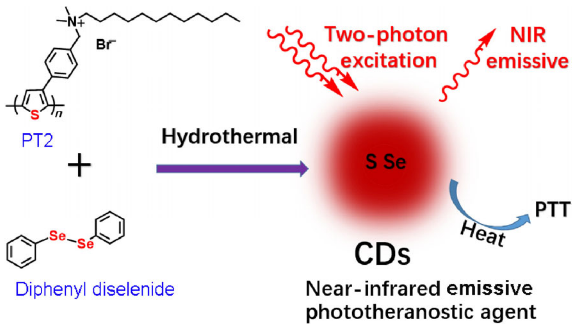

Scheme 1 Preparation and working mechanism of two-photon-excited NIR-emissive S, Se-codoped CDs.

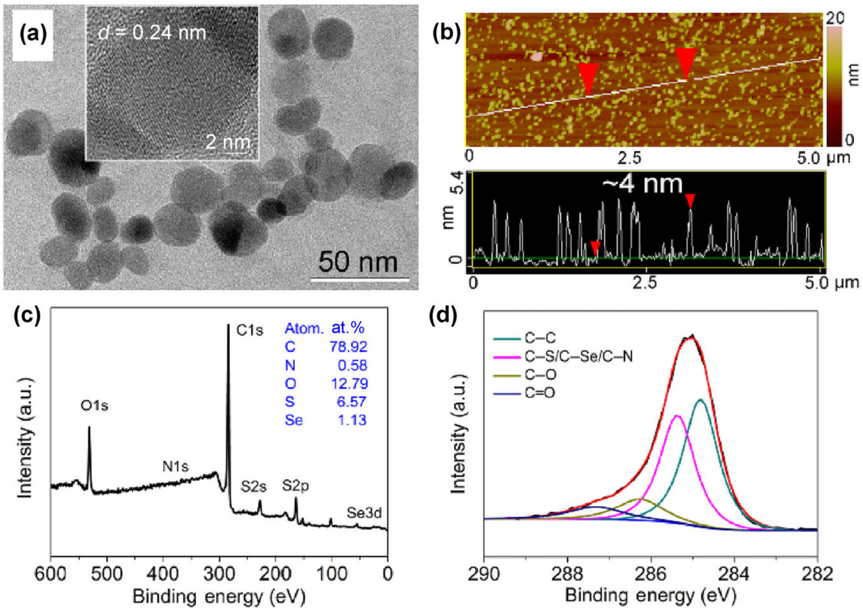

Figure 1 (a) TEM image of the CDs. The inset shows an HRTEM image of a CD. (b) AFM image and section analysis of CDs distributed on a silica substrate. (c) XPS survey spectrum of CDs. (d) Deconvolution of the high-resolution C1s XPS spectrum.

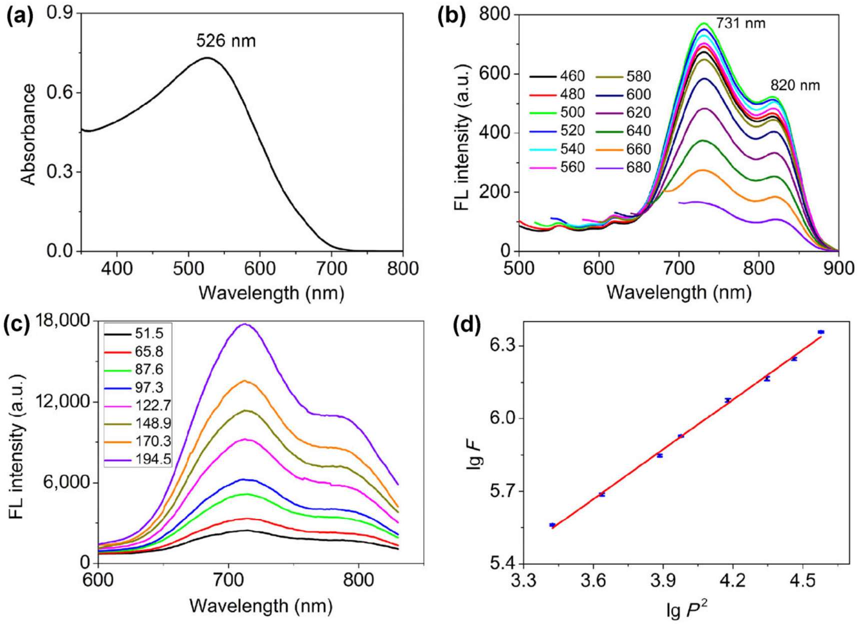

Figure 2 (a) UV–vis absorption spectrum of the CDs in the aqueous solution. (b) Fluorescence spectra of the CDs obtained as the excitation wavelength was increased from 460 to 680 nm in increments of 20 nm. (c) TPE fluorescence spectra (λ_{ex} = 880 nm) of the CD aqueous solution obtained with different laser powers (51.5 to 194.5 mW). (d) Quadratic relationship between the integrated fluorescence area and the excitation laser power at 880 nm, according to three independent measurements.

under 460-nm excitation (Fig. 2(b)). The intrinsically NIR emissions may have originated from the bandgap opening induced by the doping of the heavy element (Se) in the graphitic lattices of CDs [36, 37]. The fluorescent quantum yield of the CD aqueous solution was measured to be ~0.2% by using Cresyl violet as a reference [38], which is far lower than those of undoped CDs (~10%) and N, S-codoped CDs (~17.5%) [39, 40]. The drastically reduced quantum yield accords with the energy-gap law [41, 42]. Although the CDs had a low quantum yield, their emission in the NIR region allowed fluorescence imaging both *in vitro* and *in vivo* (as discussed below). Moreover, the difference between the maximum emission and absorption wavelength of the CDs was 205 nm. This may have minimized the self-absorption and measurement interference between the excitation and scattered light, which is beneficial for applications in fluorescence imaging [43]. Another notable feature of the CDs is that the fluorescence emission wavelengths remained almost unchanged as the excitation wavelength was increased from 460 to 680 nm in increments of 20 nm. The excitation wavelength-independent emission characteristics are attributed to the homogeneous microstructure and surface chemical states of the CDs, which caused their uniform lowest singlet state [44]. The time-resolved fluorescence spectrum of the CD aqueous solution (Fig. S4 in the ESM) suggests that the luminescence of the CDs was in the fluorescence mode and that multiple decay routes existed in the fluorescence [45, 46]. The CDs also exhibited excellent photostability and photochemical stability (Fig. S5 in the ESM), which benefits their biological and biomedical applications.

The TPE optical properties of the CD aqueous solution were investigated using a femtosecond pulsed laser. Figure 2(c) shows the TPE fluorescence spectra of the CDs under 880-nm laser excitation at different powers. With the increase of the laser power, the fluorescence intensity increased. The quadratic relationship between the fluorescence intensity of the CD aqueous solution and the excitation power, which is shown in Fig. 2(d), confirms the TPE of the CDs. The TPA cross section at 880 nm was measured to be 30,045 GM (1 GM = 10^{-50} $cm^4 \cdot s/photon$) by using fluorescein (in pH = 11 aqueous solution) as a reference. This value is two orders of magnitude larger than that of organic PSs and is comparable to that of semiconductor QDs [47, 48]. The results indicate that with heavy elements (S and Se) doped into the graphitic lattice, the large π-conjugated systems of the CDs and the enhanced intramolecular charge transfer of the CDs with the surface quaternary ammonium yielded a large TPA cross section [49]. The TPA obtained here is comparable to that of N-doped CDs [50, 51].

3.3 Photothermal conversion capability of CDs

In contrast to our previously reported N, S-codoped graphene quantum dots, which had a high singlet-O generation quantum yield [14], the S, Se-codoped CDs could not generate singlet O (Fig. S6 in the ESM). Instead, the CDs exhibited a strong capability for converting light energy into heat. Figures 3(a) and 3(b) show the temperature increase of CD aqueous solutions with different concentrations (40, 80, and 160 ppm) under 635-nm laser irradiation. The temperature of the solutions increased by 22–30 °C after 10 min of irradiation, whereas the temperature of pure water (without CDs) increased by only 10 °C. The photothermal conversion efficiency of the CDs was calculated to be ~58.2% (Fig. S7 in the ESM), which is comparable to that of Au nanostructures (~60%). More importantly, the photothermal conversion capability of the CDs exhibited excellent stability; even after 10 cycles of switching the laser on and off, a temperature elevation of ~30 °C was achieved in 10 min (Fig. 3(c)).

The manipulation of the exited energy states in the CDs by S and Se co-doping accounts for their inability to generate singlet O and their high photothermal conversion efficiency. For the large π–π conjugated structure, the energy gap ($E_{S_1-T_1}$) between the excited singlet state (S_1) and the triplet state (T_1) was larger than 0.84 eV [52]. The S_1 energy of the S, Se-codoped CDs was calculated to be ~1.51 eV, and the T_1 energy was accordingly estimated to be <0.67 eV, which is smaller than the energy required for sensitizing ground-state O (0.95 eV). Thus, no singlet O was generated by the S, Se-codoped CDs, and the absorbed light energy was mainly converted into heat.

3.4 *In vitro* imaging and PTT

The toxicity of the CDs to HeLa cells in the dark and under irradiation was investigated using the standard methyl thiazolyl tetrazolium (MTT) assay. Quantitative evaluation showed that >80% of the cells treated with CDs at a high concentration of 40 μg/mL remained alive after 24 h of incubation (Fig. 3(d), black histograms). However, the cell viability decreased to 76% when the cells were irradiated by a 635-nm laser for 5 min. Increasing the irradiation time to 10 min induced significant cell death (cell viability of <10%). The PTT effects and cell-death mechanism were investigated via flow cytometry. As shown in Fig. S8 of the ESM, the PTT treatment induced significant necrosis and

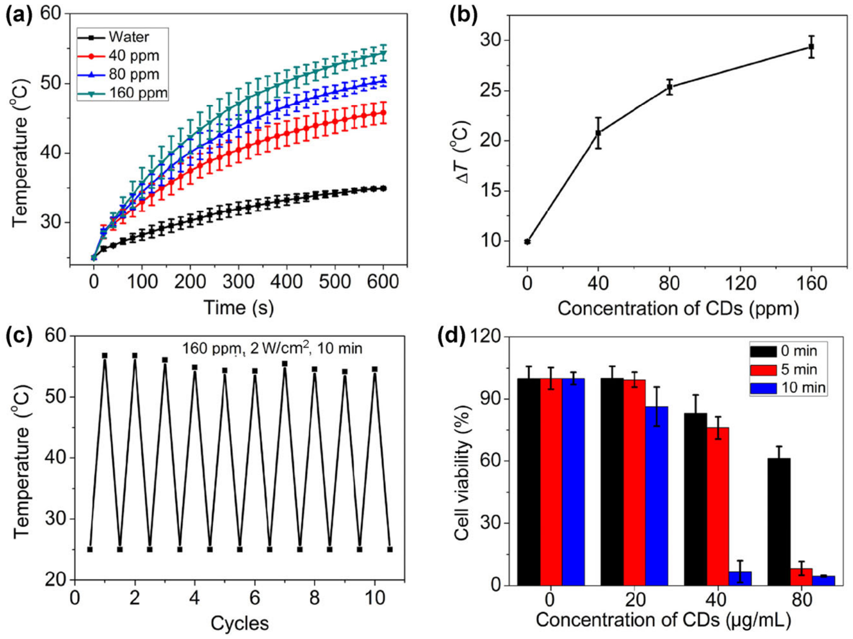

Figure 3 (a) Temperature increase of water and CD solutions with CD concentrations of 40, 80, and 160 ppm with respect to the irradiation time (635-nm laser, 2 W/cm^2). (b) Plot of the temperature change (ΔT) after irradiation for 10 min vs. the CD concentration. (c) Temperature variation of the CD solution over 10 on/off cycles of 635-nm laser irradiation. (d) Viability of HeLa cells incubated with CD solutions of different concentrations for 24 h after irradiation by the 635-nm laser (2 W/cm^2) for 0, 5, and 10 min, respectively.

apoptosis of HeLa cells (37.67% vs. 13.49% for control group). The viabilities of cells treated with CDs or laser irradiation alone did not change as significantly as the control group, indicating the strong cytotoxicity of the CDs under laser irradiation. Moreover, the toxicity of the CDs to A549 and KB cells in the dark and under irradiation was investigated using the standard MTT assay (Fig. S9 in the ESM). The dependence of the cell viability on the CD concentration and laser irradiation for these two types of cancer cells was similar to that for the case of the HeLa cells.

To investigate the capability of the CDs for simultaneous TPE fluorescence imaging and PTT, we performed an *in vitro* phototheranostic study involving two-photon laser scanning confocal microscopy using HeLa cells. As shown in Figs. 4(a) and 4(b), after 8 h of incubation with CDs, the HeLa cells exhibited clear red fluorescence under laser excitation of either 488 nm (OPE) or 880 nm (TPE). The two images correspond to the same region. Compared with the OPE, the TPE yielded a higher resolution for the CDs in the cells. The TPE PTT efficiency was assessed by monitoring the morphological changes of the HeLa cells. As shown in Figs. 4(c) and 4(d), after 3 min of irradiation by an 880-nm laser, numerous blebs had formed around the cells (red arrow). In contrast, in the absence of the CDs, no obvious change in the cell morphology was observed after 880-nm laser irradiation (Fig. S10 in the ESM). These results confirm that the experimental lasers used were safe for the cells and that the cell death was induced by the CDs.

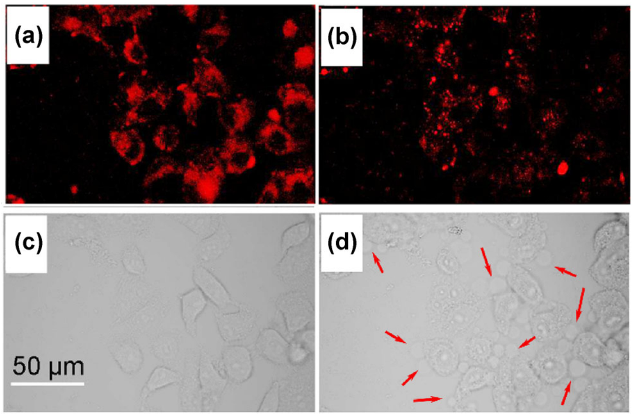

Figure 4 Confocal fluorescent microscopy images of HeLa cells incubated with CDs under (a) 488-nm and (b) 880-nm laser excitation. Transmission images of HeLa cells incubated with CDs (c) before and (d) after 3 min of 880-nm laser irradiation. All the images correspond to the same region.

3.5 *In vivo* imaging and PTT

The *in vivo* biocompatibility and histopathological behavior of the CDs were evaluated. The major organs—including the hearts, livers, spleens, lungs, and kidneys—of the two experimental groups of mice were harvested and analyzed in comparison with the control group 14 d after the mice were intravenously injected with CDs, as shown in Fig. S11 in the ESM. No obvious organ damage was observed in the CD-treated group. In addition to the histopathological examination, the liver and kidney functions of the two groups of mice were evaluated by testing the serum levels of alanine aminotransferase, aspartate aminotransferase, alkaline phosphatase, blood urea N, creatinine, and uric acid, as shown in Table S1 of the ESM. The CDs did not affect the functions of the liver or kidney. Moreover, the blood-count data were all in the normal range after the CD treatment (Table S2 in the ESM). These results indicate the excellent *in vivo* biocompatibility of the as-prepared CDs.

To investigate the *in vivo* fluorescence imaging capability of the CDs, 80 μL of the CD aqueous solution was injected into a tumor. As presented in Fig. 5(a), under 560-nm laser excitation, strong fluorescence was observed in the tumor. The background signal produced by the mouse skin was negligible. To reveal the TPE PTT effects of the CDs, comparative *in vivo* studies were performed by using the 880-nm laser as the illumination source. Here, Balb/c nude mice bearing subcutaneous 4T1 murine breast-cancer cells were randomly divided into four groups. For the PTT group, the mice were intratumorally injected with CDs (80 μL, 1 mg/mL) and then irradiated by the 880-nm laser for 10 min (group name: CDs + light). The control groups included mice injected with the same dose of CDs, without laser irradiation (group name: CDs); mice irradiated by the laser, without CD injection (group name: Light); and mice injected with saline, without laser irradiation (group name: Saline). During the laser treatment, full-body IR thermal images were obtained using an IR camera. IR thermal images with a high contrast were obtained (Fig. 5(b)). The tumor region injected with CDs exhibited a larger temperature increase under irradiation. In contrast, a substantially smaller temperature change was detected for the Saline group. The temperature of the irradiated area was recorded with respect to the irradiation time (Fig. 5(c)). For the Saline group, the surface temperature of the tumor increased by 5–6 °C after 6 min of

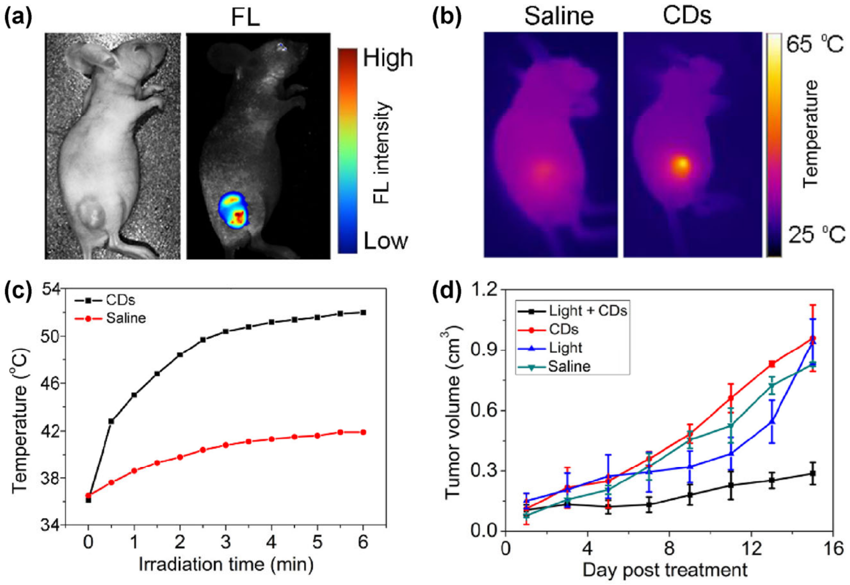

Figure 5 (a) Bright-field image (left) and fluorescence image (right) of mice after subcutaneous injection of the CD aqueous solution (1 mg/mL, 80 μL). The excitation wavelength was 560 nm, and the collected fluorescence channel was 600–900 nm. (b) IR thermal images of 4T1 tumor-bearing mice exposed to the 880-nm laser for 6 min after the injection of saline (80 μL, the left mouse) and CDs (1 mg/mL, 80 μL, the right mouse). (c) Time-dependent temperature changes of tumors injected with saline or the CD aqueous solution after 880-nm laser irradiation. (d) Time-dependent tumor volumes after different treatments.

irradiation and remained below 42 °C. However, for the mice injected with CDs, the tumor surface temperature increased rapidly and reached ~52 °C after 6 min of irradiation.

Statistical analysis was performed on the four groups by comparing the average tumor sizes during the treatment procedure. The tumor sizes were measured using a caliper every other day. As shown in Fig. 5(d), the tumor growth for the PTT group was inhibited, whereas the tumors for the control groups grew significantly during the study period, indicating that neither laser irradiation nor CD injection alone inhibited the tumor growth. These results indicate that cancer cells can be efficiently killed *in vivo* by the high temperature generated via exposure of the CDs to laser irradiation and suggest that the CDs have great potential as TPE PTAs.

4 Conclusions

S, Se-codoped CDs were synthesized by using polythiophene and diphenyl diselenide as the C source. The CDs had a platelet morphology with a graphitic structure. The CD aqueous solution exhibited excitation wavelength-independent NIR emissions. Moreover, the CDs had a large TPA cross section (~30,045 GM) at 880 nm, which allowed NIR-to-NIR photoluminescence. They exhibited a high photothermal conversion efficiency (58.2%). Owing to their collective outstanding properties—including broad absorption, good aqueous dispersibility, high photostability and pH stability, and favorable biocompatibility—the CDs are a promising multifunctional nanoplatform for the simultaneous TPE fluorescence imaging and highly efficient PTT of cancer cells *in vitro* and *in vivo*. This work may introduce a new path for the biomedical application of CDs as PTAs for cancer diagnosis and treatment.

Acknowledgements

This work was supported by the General Research Fund of Hong Kong (No. 11338516), and the National Natural Science Foundation of China (Nos. 51572269 and 51672230).

Electronic Supplementary Material: Supplementary material (detailed characteristics of CDs (particle size distribution histogram, DLS analysis, zeta potential measurement, high-resolution N1s, S2p and Se3d XPS spectra of CDs, FT-IR spectrum, time-resolved fluorescence decay of CDs), the chemo-stability and photostability of CDs, the photothermal conversion efficiency data, confocal bright-field images of HeLa cells in the absence of CDs, flow cytometry analysis of HeLa cells, MTT results of A549 and KB cells, blood analysis, liver and kidney functions of mice, H&E staining images) is available in the online version of this article at https://doi.org/10.1007/s12274-017-1528-0.

References

[1] Chen, G. Y.; Roy, I.; Yang, C. H.; Prasad, P. N. Nanochemistry and nanomedicine for nanoparticle-based diagnostics and therapy. *Chem. Rev.* **2016**, *116*, 2826–2885.

[2] Lucky, S. S.; Soo, K. C.; Zhang, Y. Nanoparticles in photodynamic therapy. *Chem. Rev.* **2015**, *115*, 1990–2042.

[3] Lim, E. K.; Kim, T.; Paik, S.; Haam, S.; Huh, Y. M.; Lee, K. Nanomaterials for theranostics: Recent advances and future challenges. *Chem. Rev.* **2015**, *115*, 327–394.

[4] Lovell, J. F.; Liu, T. W. B.; Chen, J.; Zheng, G. Activatable photosensitizers for imaging and therapy. *Chem. Rev.* **2010**, *110*, 2839–2857.

[5] Cheng, L.; Wang, C.; Feng, L. Z.; Yang, K.; Liu, Z. Functional nanomaterials for phototherapies of cancer. *Chem. Rev.* **2014**, *114*, 10869–10939.

[6] Yuan, Y. Y.; Zhang, C. J.; Xu, S. D.; Liu, B. A self-reporting AIE probe with a built-in singlet oxygen sensor for targeted photodynamic ablation of cancer cells. *Chem. Sci.* **2016**, *7*, 1862–1866.

[7] Yuan, Y. Y.; Zhang, C. J.; Kwok, R. T. K.; Xu, S. D.; Zhang, R. Y.; Wu, J. E.; Tang, B. Z.; Liu, B. Light-up probe for targeted and activatable photodynamic therapy with real-time *in situ* reporting of sensitizer activation and therapeutic responses. *Adv. Funct. Mater.* **2015**, *25*, 6586–6595.

[8] Jin, C. S.; Lovell, J. F.; Chen, J.; Zheng, G. Ablation of hypoxic tumors with dose-equivalent photothermal, but not photodynamic, therapy using a nanostructured porphyrin assembly. *ACS Nano* **2013**, *7*, 2541–2550.

[9] Yang, X.; Yang, M. X.; Pang, B.; Vara, M.; Xia, Y. N. Gold nanomaterials at work in biomedicine. *Chem. Rev.* **2015**, *115*, 10410–10488.

[10] Wang, K. K.; Zhang, Y. F.; Wang, J.; Yuan, A. H.; Sun, M. J.; Wu, J. H.; Hu, Y. Q. Self-assembled IR780-loaded transferrin

nanoparticles as an imaging, targeting and PDT/PTT agent for cancer therapy. *Sci. Rep.* **2016**, *6*, 27421.

[11] Pang, X. J.; Wang, J. P.; Tan, X. X.; Guo, F.; Lei, M. Z.; Ma, M.; Yu, M.; Tan, F. P.; Li, N. Dual-modal imaging-guided theranostic nanocarriers based on indocyanine green and mTOR inhibitor rapamycin. *ACS Appl. Mater. Interfaces* **2016**, *8*, 13819–13829.

[12] Shi, C. H.; Wu, J. B.; Pan, D. F. Review on near-infrared heptamethine cyanine dyes as theranostic agents for tumor imaging, targeting, and photodynamic therapy. *J. Biomed. Opt.* **2016**, *21*, 050901.

[13] Li, N.; Zhao, P. X.; Astruc, D. Anisotropic gold nanoparticles: Synthesis, properties, applications, and toxicity. *Angew. Chem., Int. Ed.* **2014**, *53*, 1756–1789.

[14] Xu, H.; Li, Q.; Wang, L. H.; He, Y.; Shi, J. Y.; Tang, B.; Fan, C. H. Nanoscale optical probes for cellular imaging. *Chem. Soc. Rev.* **2014**, *43*, 2650–2661.

[15] Ge, J. C.; Lan, M. H.; Zhou, B. J.; Liu, W. M.; Guo, L.; Wang, H.; Jia, Q. Y.; Niu, G. L.; Huang, X.; Zhou, H. Y. et al. A graphene quantum dot photodynamic therapy agent with high singlet oxygen generation. *Nat. Commun.* **2014**, *5*, 4596.

[16] Ge, J. C.; Jia, Q. Y.; Liu, W. M.; Guo, L.; Liu, Q. Y.; Lan, M. H.; Zhang, H. Y.; Meng, X. M.; Wang, P. F. Red-emissive carbon dots for fluorescent, photoacoustic, and thermal theranostics in living mice. *Adv. Mater.* **2015**, *27*, 4169–4177.

[17] Cao, L.; Meziani, M. J.; Sahu, S.; Sun, Y. P. Photoluminescence properties of graphene versus other carbon nanomaterials. *Acc. Chem. Res.* **2013**, *46*, 171–180.

[18] Morimoto, Y.; Horie, M.; Kobayashi, N.; Shinohara, N.; Shimada, M. Inhalation toxicity assessment of carbon-based nanoparticles. *Acc. Chem. Res.* **2013**, *46*, 770–781.

[19] Lim, S. Y.; Shen, W.; Gao, Z. Q. Carbon quantum dots and their applications. *Chem. Soc. Rev.* **2015**, *44*, 362–381.

[20] Baker, S. N.; Baker, G. A. Luminescent carbon nanodots: Emergent nanolights. *Angew. Chem., Int. Ed.* **2010**, *49*, 6726–6744.

[21] Zeng, J.; Goldfeld, D.; Xia, Y. N. A plasmon-assisted optofluidic (PAOF) system for measuring the photothermal conversion efficiencies of gold nanostructures and controlling an electrical switch. *Angew. Chem., Int. Ed.* **2013**, *52*, 4169–4173.

[22] Ji, M. W.; Xu, M.; Zhang, W.; Yang, Z. Z.; Huang, L.; Liu, J. J.; Zhang, Y.; Gu, L.; Yu, Y. X.; Hao, W. C. et al. Structurally well-defined Au@$Cu_{2-x}S$ core–shell nanocrystals for improved cancer treatment based on enhanced photothermal efficiency. *Adv. Mater.* **2016**, *28*, 3094–3101.

[23] Song, J. B.; Wang, F.; Yang, X. Y.; Ning, B.; Harp, M. G.; Culp, S. H.; Hu, S.; Huang, P.; Nie, L. M.; Chen, J. Y. et al. Gold nanoparticle coated carbon nanotube ring with enhanced Raman scattering and photothermal conversion property for theranostic applications. *J. Am. Chem. Soc.* **2016**, *138*, 7005–7015.

[24] Hu, Y.; Wang, R. Z.; Wang, S. G.; Ding, L.; Li, J. C.; Luo, Y.; Wang, X. L.; Shen, M. W.; Shi, X. Y. Multifunctional Fe_3O_4 @ Au core/shell nanostars: A unique platform for multimode imaging and photothermal therapy of tumors. *Sci. Rep.* **2016**, *6*, 28325.

[25] Li, D.; Han, D.; Qu, S. N.; Liu, L.; Jing, P. T.; Zhou, D.; Ji, W. Y.; Wang, X. Y.; Zhang, T. F.; Shen, D. Z. Supra-(carbon nanodots) with a strong visible to near-infrared absorption band and efficient photothermal conversion. *Light: Sci. Appl.* **2016**, *5*, e16120.

[26] Hu, S. L.; Trinchi, A.; Atkin, P.; Cole, I. Tunable photoluminescence across the entire visible spectrum from carbon dots excited by white light. *Angew. Chem., Int. Ed.* **2015**, *54*, 2970–2974.

[27] Tang, L. B.; Ji, R. B.; Li, X. M.; Bai, G. X.; Liu, C. P.; Hao, J. H.; Lin, J. Y.; Jiang, H. X.; Teng, K. S.; Yang, Z. B. et al. Deep ultraviolet to near-infrared emission and photoresponse in layered N-doped graphene quantum dots. *ACS Nano* **2014**, *8*, 6312–6320.

[28] Wu, L.; Luderer, M.; Yang, X. X.; Swain, C.; Zhang, H. Y.; Nelson, K.; Stacy, A. J.; Shen, B. Z.; Lanza, G. M.; Pan, D. J. Surface passivation of carbon nanoparticles with branched macromolecules influences near infrared bioimaging. *Theranostics* **2013**, *3*, 677–686.

[29] Shen, Y. Z.; Shuhendler, A. J.; Ye, D. J.; Yu, J. J.; Chen, H. Y. Two-photon excitation nanoparticles for photodynamic therapy. *Chem. Soc. Rev.* **2016**, *45*, 6725–6741.

[30] Cao, L.; Wang, X.; Meziani, M. J.; Lu, F. S.; Wang, H. F.; Luo, P. G.; Lin, Y.; Harruff, B. A.; Veca, L. M.; Murray, D. et al. Carbon dots for multiphoton bioimaging. *J. Am. Chem. Soc.* **2007**, *129*, 11318–11319.

[31] Fowley, C.; McHale, A. P.; McCaughan, B.; Fraix, A.; Sortino, S.; Callan, J. F. Carbon quantum dot-NO photoreleaser nanohybrids for two-photon phototherapy of hypoxic tumors. *Chem. Commun.* **2015**, *51*, 81–84.

[32] Wang, J.; Zhang, Z. H.; Zha, S.; Zhu, Y. Y.; Wu, P. Y.; Ehrenberg, B.; Chen, J. Y. Carbon nanodots featuring efficient FRET for two-photon photodynamic cancer therapy with a low fs laser power density. *Biomaterials* **2014**, *35*, 9372–9381.

[33] Li, J. L.; Bao, H. C.; Hou, X. L.; Sun, L.; Wang, X. G.; Gu, M. Graphene oxide nanoparticles as a nonbleaching optical probe for two-photon luminescence imaging and cell therapy. *Angew. Chem., Int. Ed.* **2012**, *51*, 1830–1834.

[34] Lan, M. H.; Wu, J. S.; Liu, W. M.; Zhang, W. J.; Ge, J. C.; Zhang, H. Y.; Sun, J. Y.; Zhao, W. W.; Wang, P. F. Copolythiophene-derived colorimetric and fluorometric sensor

for visually supersensitive determination of lipopolysaccharide. *J. Am. Chem. Soc.* **2012**, *134*, 6685–6694.

[35] Guo, X.; Wang, C. F.; Yu, Z. Y.; Chen, L.; Chen, S. Facile access to versatile fluorescent carbon dots toward light-emitting diodes. *Chem. Commun.* **2012**, *48*, 2692–2694.

[36] Kozák, O.; Sudolská, M.; Pramanik, G.; Cígler, P.; Otyepka, M.; Zbořil, R. Photoluminescent carbon nanostructures. *Chem. Mater.* **2016**, *28*, 4085–4128.

[37] Yang, S. W.; Sun, J.; Li, X. B.; Zhou, W.; Wang, Z. Y.; He, P.; Ding, G. Q.; Xie, X. M.; Kang, Z. H.; Jiang, M. H. Large-scale fabrication of heavy doped carbon quantum dots with tunable-photoluminescence and sensitive fluorescence detection. *J. Mater. Chem. A* **2014**, *2*, 8660–8667.

[38] Brouwer, A. M. Standards for photoluminescence quantum yield measurements in solution (IUPAC technical report). *Pure Appl. Chem.* **2011**, *83*, 2213–2228.

[39] Yang, F.; Zhao, M. L.; Zheng, B. Z.; Xiao, D.; Wu, L.; Guo, Y. Influence of pH on the fluorescence properties of graphene quantum dots using ozonation pre-oxide hydrothermal synthesis. *J. Mater. Chem.* **2012**, *22*, 25471–25479.

[40] Zhao, S. J.; Lan, M. H.; Zhu, X. Y.; Xue, H. T.; Ng, T.-W.; Meng, X. M.; Lee, C.-S.; Wang, P. F.; Zhang, W. J. Green synthesis of bifunctional fluorescent carbon dots from garlic for cellular imaging and free radical scavenging. *ACS Appl. Mater. Interfaces* **2015**, *7*, 17054–17060.

[41] Turro, N. J. *Modern Molecular Photochemistry;* University Science Books: Mill Valley, CA, 1991.

[42] Englman, R.; Jortner, J. The energy gap law for radiationless transitions in large molecules. *J. Mol. Phys.* **1970**, *18*, 145–164.

[43] Lan, M. H.; Zhang, J. F.; Zhu, X. Y.; Wang, P. F.; Chen, X. F.; Lee, C. S.; Zhang, W. J. Highly stable organic fluorescent nanorods for living-cell imaging. *Nano Res.* **2015**, *8*, 2380–2389.

[44] Sharma, A.; Gadly, T.; Gupta, A.; Ballal, A.; Ghosh, S. K.; Kumbhakar, M. Origin of excitation dependent fluorescence in carbon nanodots. *J. Phys. Chem. Lett.* **2016**, *7*, 3695–3702.

[45] Xu, Q. F.; Zhou, Q.; Hua, Z.; Xue, Q.; Zhang, C. F.; Wang, X. Y.; Pan, D. Y.; Xiao, M. Single-particle spectroscopic measurements of fluorescent graphene quantum dots. *ACS Nano* **2013**, *7*, 10654–10661.

[46] Khan, S.; Gupta, A.; Verma, N. C.; Nandi, C. K. Time-resolved emission reveals ensemble of emissive states as the origin of multicolor fluorescence in carbon dots. *Nano Lett.* **2015**, *15*, 8300–8305.

[47] Singh, S.; Aggarwal, A.; Bhupathiraju, N. V. S. D. K.; Arianna, G.; Tiwari, K.; Drain, C. M. Glycosylated porphyrins, phthalocyanines, and other porphyrinoids for diagnostics and therapeutics. *Chem. Rev.* **2015**, *115*, 10261–10306.

[48] Pu, S. C.; Yang, M. J.; Hsu, C. C.; Lai, C. W.; Hsieh, C. C.; Lin, S. H.; Cheng, Y. M.; Chou, P. T. The empirical correlation between size and two-photon absorption cross section of CdSe and CdTe quantum dots. *Small* **2006**, *2*, 1308–1313.

[49] Liu, Q.; Guo, B. D.; Rao, Z. Y.; Zhang, B. H.; Gong, J. R. Strong two-photon-induced fluorescence from photostable, biocompatible nitrogen-doped graphene quantum dots for cellular and deep-tissue imaging. *Nano Lett.* **2013**, *13*, 2436–2441.

[50] Kong, B.; Zhu, A. W.; Ding, C. Q.; Zhao, X. M.; Li, B.; Tian, Y. Carbon dot-based inorganic–organic nanosystem for two-photon imaging and biosensing of pH variation in living cells and tissues. *Adv. Mater.* **2012**, *24*, 5844–5848.

[51] Peng, X. J.; Yang, Z. G.; Wang, J. Y.; Fan, J. L.; He, Y. X.; Song, F. L.; Wang, B. S.; Sun, S. G.; Qu, J. L.; Qi, J. et al. Fluorescence ratiometry and fluorescence lifetime imaging: Using a single molecular sensor for dual mode imaging of cellular viscosity. *J. Am. Chem. Soc.* **2011**, *133*, 6626–6635.

[52] Fan, M.; Yao, J.; Tung, C.-H. *Molecular Photochemistry and Materials Science;* Chinese Science Publishing & Media Ltd.: Beijing, 2008. (in Chinese)